J. Fluid Mech. (2014), *vol.* 746, *pp.* 273–299. © Cambridge University Press 2014
doi:10.1017/jfm.2014.120

Slender axisymmetric Stokesian swimmers

S. Toppaladoddi[1,2,†] **and N. J. Balmforth**[3]

[1]Mathematical Institute, University of Oxford, Andrew Wiles Building, Woodstock Road, Oxford OX2 6GG, UK

[2]Department of Geology & Geophysics, Yale University, P.O. Box 208109, New Haven, CT 06520-8109, USA

[3]Department of Mathematics, University of British Columbia, 1984 Mathematics Road, Vancouver, BC, V6T 1Z2, Canada

(Received 29 July 2013; revised 2 January 2014; accepted 28 February 2014; first published online 1 April 2014)

Slender-body theory is used to study axisymmetric swimmers propelled by motions of their surfaces. To leading order, the locomotion speed is given by an integral involving the fluid velocity at the surface of the slender body. Locomotion speeds are calculated for fixed-shape swimmers with prescribed fluid surface velocities and for impermeable swimmers driven by propagating surface waves. Next, the internal mechanics is considered, modelling the swimmer as a viscous fluid bounded by an elastic shell. Prescribed forces are exerted on the shell to drive both the internal and external fluid flow and the surface waves. The internal fluid mechanics is determined using lubrication theory. Locomotion speeds are calculated for transverse and longitudinal waves of surface deformation, and the efficiency of the motions is determined. Transverse surface waves are both weaker and less efficient at driving locomotion than longitudinal waves. The results indicate how estimates of swimming speed based on nearly spherical swimmers with low-amplitude surface waves can be adapted for slender swimmers with nonlinear surface deformations.

Key words: low-Reynolds-number flows, propulsion, slender-body theory

1. Introduction

Microscopic organisms can propel themselves in viscous fluid by creating travelling waves along their surfaces. Taylor's (1951) wavy two-dimensional sheet provided one of the first theoretical models, determining the speed of locomotion for low-amplitude waves. Taylor's analysis was subsequently extended to different geometries by Lighthill (1952) and Blake (1971*a*,*b*,*c*), who studied the locomotion of spheres and cylinders. More recent developments are reviewed by Lauga & Powers (2009).

In the current study, we extend Taylor's analysis by exploring the propulsion of slender axisymmetrical bodies. The motivation for considering such swimmers comes in part from observations of the cyanobacterium *Synechococcus*, whose mechanism for propulsion currently remains mysterious (Brahamsha 1999; Jarrell & McBride 2008). These organisms are somewhat long and cylindrical, the typical aspect ratio (of radius to length) being approximately 1/4. Moreover, they possess neither cilia nor

† Email address for correspondence: srikanth.toppaladoddi@yale.edu

https://doi.org/10.1017/jfm.2014.120 Published online by Cambridge University Press

flagella, the appendages that often assist many micro-organisms in their movement. Instead, Ehlers *et al.* (1996) suggested that the locomotion might be due to undetected axisymmetrical travelling waves of surface deformation (see also Stone & Samuel 1996). These authors modelled the bacterium as a sphere; accounting for a slender geometry is one of our current aims. More recent discussions have refined this interpretation of what propels *Synechococcus*, proposing that helical motions on the bacterium's surface may be responsible (Ehlers & Oster 2012). Nevertheless, a necessary first step in improving the modelling is to explore the effect of the swimmer's shape on locomotion driven by the simplest type of surface waves.

Further biological motivation is provided by strategies for cell migration based on surface shape changes such as 'pseudopods' and 'blebs' (propagating surface protrusions: Charras & Palluch 2008; Barry & Bretscher 2010; Van Haastert 2011; Driscoll *et al.* 2012; Allard & Mogilner 2013). In particular, wave-like pseudopods have been suggested to propel amoeba in viscous fluid. Despite the relatively elongated shape of many of these organisms, the only models proposed to date are either again based on deforming spheroids (Farutin *et al.* 2013), or numerically simulate the Stokes flow around an object with prescribed surface deformation (Arroyo *et al.* 2012). Specific slender swimmers for which our study is relevant include *Dictyostelium* (Barry & Bretscher 2010; Van Haastert 2011) and *Eutreptiella* cells (Fletcher & Theriot 2004; Arroyo *et al.* 2012).

A different motivation is provided by the robotic swimmer of Setter, Bucher & Haber (2012); see also Palagi *et al.* (2013) and Setter & Bucher (2013, 2014). This device consists of a tube containing a motor driving wave-like normal surface displacements, and was designed as a cylindrical analogue of Taylor's sheet. To gauge the suitability of such slender robotic devices to various applications, it is important to compare the efficiency of different swimmers and their strokes. Setter and coworkers provide a theoretical analysis paralleling Taylor's work, exploring how axisymmetric low-amplitude surface waves propel an infinite cylinder (cf. Blake 1971*b*). In practise, any such object has finite length, but accounting for the ends complicates the modelling. We deal with such complications here by considering the limit of a slender swimmer in which asymptotic methods can be used to take into account a finite length and to consider general axisymmetrical surface shapes and wave profiles.

Our asymptotic analysis is based on the slender-body theory developed for Stokes flow around axisymmetrical objects (Tuck 1964; Cox 1970; Tillett 1970; Keller & Rubinow 1976; Johnson 1980); some more recent developments and references are summarised by Blake, Tuck & Wakeley (2010). Section 2 provides a summary of the theory as it applies in the current situation, although the analysis is mostly a special case of more general theory provided previously. To leading order, the analysis provides a concise, integral formula for the locomotion speed, a result relying on the slenderness of the body, but not on any assumption on the amplitude of the surface deformations. Indeed, the amplitudes can be nonlinear and as large as the radius of the body itself, thereby eliminating one of the limitations of the analyses styled after Taylor's work.

The slender-body formula offers a convenient means to compute locomotion speeds given prescribed surface velocities, as we illustrate in §§ 3 and 4. This allows us to collect together a number of results connected to previous models (Blake 1971*b*; Keller & Wu 1977; Leshansky *et al.* 2007; Saintillan & Shelley 2007; Kanevsky, Shelley & Tornberg 2010; Spagnolie & Lauga 2010; Setter *et al.* 2012) within a common theoretical framework, albeit for the special slender geometry. Specifically, § 3 discusses swimmers with a fixed shape, but having fluid flow at their surfaces

https://doi.org/10.1017/jfm.2014.120 Published online by Cambridge University Press

because that interface is either in tangential motion or permeable. Section 4 discusses swimmers propelled by propagating waves of surface deformation. Unfortunately, prescribing the surface velocity in this fashion ignores the internal mechanics of the swimmer. Indeed, estimates of the efficiency of the swimming stroke may be inadequate in such a model, as the interior of the swimmer must deform in order to generate fluid motion at its surface and the resulting internal dissipation is ignored entirely. This omission is particularly acute in the slender limit where internal shear rates are much larger than those driven externally.

To avoid this problem, in § 5, we present an idealised model incorporating the internal mechanics, assuming that the swimmer is a thin elastic shell filled with viscous fluid. To activate motion, prescribed forces are exerted on the surface, such as would be incurred if there were a network of 'muscle' fibres, either stretched diametrically across each cross-section of the swimmer and tethered at the surface, or embedded within it and orientated axially (although we present no details, we also briefly mention how alternative mechanisms for actuating surface motion can be incorporated within the model). The fibres, or whatever structures generate the forcing, are assumed to be sufficiently dense that they provide axisymmetrical transverse or longitudinal forces on the surface, but are either too thin or organised in such a way that they do not impede internal fluid flow. We use lubrication theory to model the flow of the viscous interior driven by the fibre forces. The profile of the resulting surface waves is then determined self-consistently as part of the solution of the problem. Importantly, because our swimmer is slender, lubrication forces inside the swimmer dominate the stresses exerted by the external fluid motions, decoupling the internal flow dynamics from the locomotion problem. Moreover, the dissipation incurred inside the swimmer exceeds that from outside, allowing us to determine the swimming efficiency. In addition to a variety of numerical solutions, we provide an analysis of a short-wavelength limit that furnishes convenient analytical results.

The internal fluid mechanics of our lubrication theory corresponds to a type of peristaltic motion (cf. Shapiro, Jaffrin & Weinberg 1969; Jaffrin & Shapiro 1971), although conventional models of peristalsis also fix the surface displacement rather than solve self-consistently for the surface motion (see Takagi & Balmforth 2011). This connection makes our study relevant to peristalsis in closed chambers (Selverov & Stone 2001; Yi, Bau & Hu 2002), the internal transport of nutrients and chemicals within organisms (Iima & Nakagaki 2012; Alim *et al.* 2013), and micromechanical pumps and mixers (Stone, Stroock & Ajdari 2004; Nakahara *et al.* 2013). A key difference between the current study and many models of these other problems is that we consider peristaltic pumping in the more biologically relevant situation of a shaped axisymmetrical structure, rather than a rectangular duct. Finally, we note that Ajdari & Stone (1999) have previously coupled together models of locomotion and peristalsis; their configuration is rather different from ours, and the connection of the two studies is largely superficial.

2. The external fluid mechanics

We begin with the Stokes equations in dimensionless form, determining the velocity field, $\boldsymbol{u}$, and pressure, P, of external fluid motions:

$$\boldsymbol{\nabla}\cdot\boldsymbol{u}=0 \quad \text{and} \quad \boldsymbol{\nabla}P=\nabla^2\boldsymbol{u}. \tag{2.1}$$

To arrive at these equations, we have scaled distance with the length of the swimmer, L, velocity with the speed of the locomotive waves, c, time with L/c, and pressure with $\mu c/L$, where μ is the external fluid's viscosity. For the spatial coordinates, we use

https://doi.org/10.1017/jfm.2014.120 Published online by Cambridge University Press

a cylindrical polar coordinate system, (r, ϑ, z), positioned in the frame of the swimmer. In this frame, the swimmer's surface is located at $r = \epsilon R(z, t)$, where $\epsilon \ll 1$ is the aspect ratio of the body, given by the ratio of its maximum radius and length. Note that we assume that the ends of the body cannot move relative to one another (fixing their position in the swimmer's frame), which rules out certain swimming strategies (Lauga & Powers 2009).

2.1. *Slender-body theory*

Following Tuck (1964), Cox (1970), Tillett (1970) and Keller & Rubinow (1976), we express the Stokes flow solution outside the slender body as a superposition of Stokeslets and sources distributed along the swimmer's axis, $0 \leqslant z \leqslant 1$ and $r = 0$:

$$\boldsymbol{u}(r, z, t) = V\hat{\boldsymbol{z}} + \int_0^1 \left[\frac{\hat{\boldsymbol{z}}}{X} + \frac{(\hat{\boldsymbol{z}}\cdot\boldsymbol{X})\boldsymbol{X}}{X^3}\right]\alpha(z')\,\mathrm{d}z' + \int_0^1 \frac{\boldsymbol{X}}{X^3}\delta(z')\,\mathrm{d}z', \tag{2.2}$$

where

$$\boldsymbol{X} = r\hat{\boldsymbol{r}} + (z - z')\hat{\boldsymbol{z}} \quad \text{and} \quad X = \sqrt{r^2 + (z - z')^2}. \tag{2.3}$$

Here, $V\hat{\boldsymbol{z}}$ is the far-field velocity field ($\boldsymbol{u} \to V\hat{\boldsymbol{z}}$ for $X \to \infty$), which, since the velocity field is written in the frame of the swimmer, is given by the locomotion speed V. Moreover, $\alpha(z)\hat{\boldsymbol{z}}$ is the Stokeslet distribution and $\delta(z)$ is the source distribution (we suppress the dependence on t to avoid cluttering the equations). Those densities are determined by imposing the boundary condition on the surface of the swimmer, $r = \epsilon R(z, t)$, i.e.

$$\boldsymbol{u}(\epsilon R, z, t) = \epsilon U(z, t)\hat{\boldsymbol{r}} + W(z, t)\hat{\boldsymbol{z}}, \tag{2.4}$$

where the two functions, $U(z, t)$ and $W(z, t)$, are prescribed later according to whether we impose the surface motion directly (§§ 3 and 4), or model the internal mechanics of the swimmer (§ 5). In general, the imposition of (2.4) leads to integral equations to solve for $\alpha(z)$ and $\delta(z)$ (e.g. Tuck 1964; Blake *et al.* 2010); we exploit the small aspect ratio, $\epsilon \ll 1$, to simplify and solve these equations as follows.

In the limit $\epsilon \to 0$, we may evaluate the nearly singular parts of the integrals in (2.2) for $r = \epsilon\rho$ with $\rho = O(1)$. In particular, working to order ϵ, we first extract the nearly singular parts of the integrals, then approximate the regular integrals by replacing X by $|z - z'|$ (see, for example, the appendices of Tuck (1964) and Keller & Rubinow (1976)):

$$\begin{aligned} u(\epsilon\rho, z, t) &= \epsilon\rho\delta\int_0^1 \frac{\mathrm{d}z'}{X^3} + \epsilon\rho\int_0^1 [\delta(z') - \delta(z) + (z - z')\alpha(z')]\frac{\mathrm{d}z'}{X^3} \\ &= \epsilon\rho\delta\int_0^1 \frac{\mathrm{d}z'}{X^3} + O(\epsilon\delta, \epsilon\alpha) \end{aligned} \tag{2.5}$$

and

$$\begin{aligned} w(\epsilon\rho, z, t) &= V + 2\int_0^1 \frac{[\alpha(z') - \alpha(z)]\,\mathrm{d}z'}{|z - z'|} + \int_0^1 \frac{[\delta(z') - \delta(z) - \delta_z(z)(z' - z)]\,\mathrm{d}z'}{|z - z'|(z - z')} \\ &\quad + \alpha\int_0^1 \left[\frac{1}{X} + \frac{(z - z')^2}{X^3}\right]\mathrm{d}z' \\ &\quad + \int_0^1 [\delta(z) + \delta_z(z)(z' - z)](z' - z)\frac{\mathrm{d}z'}{X^3} + O(\epsilon\alpha, \epsilon\delta), \end{aligned} \tag{2.6}$$

https://doi.org/10.1017/jfm.2014.120 Published online by Cambridge University Press

where we have used subscripts to denote partial derivatives. For the singular integrals,

$$\int_0^1 \frac{\mathrm{d}z'}{X} = -2\log(\epsilon\rho) + \log[4z(1-z)] + O(\epsilon^2), \tag{2.7}$$

$$\int_0^1 \frac{\mathrm{d}z'}{X^3} = \frac{2}{\epsilon^2\rho^2} + O(1), \quad \int_0^1 \frac{(z-z')^2\,\mathrm{d}z'}{X^3} = \int_0^1 \frac{\mathrm{d}z'}{X} - 2 + O(\epsilon^2) \tag{2.8}$$

and

$$\int_0^1 \frac{(z'-z)\,\mathrm{d}z'}{X^3} = \frac{(2z-1)}{z(1-z)} + O(\epsilon^2). \tag{2.9}$$

Thus, to $O(\epsilon\delta, \epsilon\alpha)$,

$$u(\epsilon\rho, z, t) \sim \frac{2\delta}{\epsilon\rho} \tag{2.10}$$

and (after some algebra involving integration by parts)

$$w(\epsilon\rho, z, t) \sim \Lambda \log\frac{\Delta}{\epsilon^2\rho^2} + V - \Lambda - \frac{\partial\delta}{\partial z} + \int_0^1 \frac{[\Lambda(z') - \Lambda(z)]\,\mathrm{d}z'}{|z-z'|}, \tag{2.11}$$

where

$$\Lambda(z) = 2\alpha - \delta_z \quad \text{and} \quad \Delta(z) = 4z(1-z). \tag{2.12}$$

The surface boundary conditions now indicate that

$$\delta = \tfrac{1}{2}\epsilon^2 RU, \tag{2.13}$$

and Λ satisfies the integral equation (cf. Tuck 1964, Keller & Rubinow 1976)

$$\Lambda \log\frac{\epsilon^2R^2}{\Delta} = V - W - \frac{\partial\delta}{\partial z} - \Lambda + \int_0^1 [\Lambda(z') - \Lambda(z)]\frac{\mathrm{d}z'}{|z'-z|}. \tag{2.14}$$

In view of (2.13), W should be $O(\epsilon^2 U)$ in order to retain both W and δ_z in (2.14).

Note that (2.13) and (2.14) imply that the velocity field near the swimmer is

$$u \sim \frac{\epsilon^2 RU}{r} \quad \text{and} \quad w \sim 2\Lambda\log\frac{\epsilon R}{r} + W, \tag{2.15}$$

and the integral of (2.14) provides the useful relation

$$V = \int_0^1 \left[W + \Lambda\log\frac{R^2}{\Delta}\right]\mathrm{d}z - 2[\delta(z)]_{z=0}^{z=1}\log\epsilon, \tag{2.16}$$

in view of the fact that the net force balance on the swimmer demands that

$$\int_0^1 \alpha(z)\,\mathrm{d}z = 0 \quad \text{or} \quad \int_0^1 \Lambda(z)\,\mathrm{d}z = -[\delta(z)]_{z=0}^{z=1}, \tag{2.17}$$

and a change of integration variable eliminates the final term in (2.14).

https://doi.org/10.1017/jfm.2014.120 Published online by Cambridge University Press

2.2. *Leading-order solution of the integral equation*

We may solve (2.14) to leading order by noting that, when $\epsilon \to 0$, the logarithmic term that appears on the left-hand side becomes large (see e.g. Cox 1970; Keller & Rubinow 1976). Thus, the main balance in (2.14) implies that

$$2\Lambda \log \epsilon \sim V - W - \delta_z. \tag{2.18}$$

The resulting solution for Λ is the leading order of an asymptotic sequence in inverse powers of $\log \epsilon$; for practical purposes, the relatively slow convergence of this series may make it preferable to solve (2.14) numerically or try other refinements (see e.g. Blake *et al.* 2010). In § 3, we persist with the full integral equation, as the examples provided there can be analysed without making the leading-order approximation in (2.18). From § 4 on, however, we resort to the leading-order results, which, after inserting (2.18) into (2.16), are encapsulated in the analytical expression for the locomotion speed,

$$V \sim \int_0^1 \left[1 - \frac{\log(R^2/\Delta)}{2\log\epsilon}\right] W \,\mathrm{d}z - \frac{\epsilon^2}{4\log\epsilon} \int_0^1 (RU)_z \log\frac{R^2}{\Delta}\,\mathrm{d}z. \tag{2.19}$$

To arrive at this relation, we have neglected the integral multiplying $V/\log\epsilon$ in comparison to the V on the left-hand side of (2.16), and omitted the final term in view of (2.13) and $R(0, t) = R(1, t) = 0$ (assuming U remains finite there). We retain both terms in the integral involving W, as this turns out to be necessary in § 4.

For purely radial motion,

$$U \equiv R_t \quad \text{and} \quad W = 0, \tag{2.20}$$

we find (recalling that $\Delta = \sqrt{4z(1-z)}$)

$$V \sim -\frac{\epsilon^2}{8\log\epsilon} \int_0^1 (R^2)_{zt} \log\frac{R^2}{\sqrt{4z(1-z)}}\,\mathrm{d}z. \tag{2.21}$$

When the solution is periodic in time, we may average (2.21) over a period and then integrate by parts to find

$$\overline{V} \sim -\frac{\epsilon^2}{2\log\epsilon} \int_0^1 \overline{R_t R_z}\,\mathrm{d}z, \tag{2.22}$$

where the temporal average is denoted by the overline.

2.3. *Efficiency*

The efficiency of a swimmer's stroke can be defined by comparing the power input required to drive the locomotion to that needed to drag the undeformed object through the fluid at the same, fixed, mean locomotion speed $\overline{V}$ (Childress 1981). The latter is given by the product of $\overline{V}$ with the dimensionless drag force,

$$F_d \sim -8\pi \int_0^1 \alpha(z)\,\mathrm{d}z \tag{2.23}$$

https://doi.org/10.1017/jfm.2014.120 Published online by Cambridge University Press

(see, for example, Keller & Rubinow (1976); our non-dimensionalisation scales their result for F_d with μcL and the Stokeslet density α with c). For the problem of rigid-body translation, the constraint (2.17) no longer applies, but (2.14) still holds with $\delta \equiv 0$. The integral of (2.14) therefore furnishes $\int_0^1 \alpha(z)\,\mathrm{d}z = \overline{V}/4\log\epsilon$ to leading order, and so the product of force and speed, or dissipation rate, is

$$D \sim 2\pi\overline{V}^2/\log(1/\epsilon). \tag{2.24}$$

We next estimate the power input required to drive the swimming stroke, assuming that no work is needed to deform the swimmer itself (an assumption that may be hard to justify, as we amplify later). The power input to the fluid is

$$\mathscr{P} = -2\pi\epsilon \int_0^1 (\sigma \cdot \boldsymbol{n}) \cdot \boldsymbol{u} R\,\mathrm{d}z, \tag{2.25}$$

where σ is the stress tensor (made dimensionless with $\mu c/L$) and $\boldsymbol{n}$ is the unit normal to the surface. The integrand of (2.25) can be split up into the two pieces,

$$\epsilon RU[2u_r - p + \epsilon R_z(w_r + u_z)] \quad \text{and} \quad RW[w_r + u_z - \epsilon R_z(2w_z - p)], \tag{2.26}$$

both evaluated at $r = \epsilon R$. We approximate each piece to leading order, assuming further that $W = O(\chi)$ and $1 \gg \chi \gg \epsilon^2\log(1/\epsilon)$, corresponding to our models for surface waves introduced later. From (2.15), bearing in mind that $\Lambda = O(1/\log\epsilon)$, we compute

$$u_r \sim -U/R, \quad u_z = O(\epsilon), \quad w_r = \frac{(W-V)}{\epsilon R\log\epsilon}, \quad w_z = O(\chi). \tag{2.27}$$

Furthermore, from the axial momentum equation, $p_z = \nabla^2 w$, we estimate that $p \sim W_z = O(\chi)$. The leading-order approximations of the two terms in (2.26) are therefore

$$2\epsilon RUu_r \sim -2\epsilon U^2 \quad \text{and} \quad RWw_r \sim \frac{W(W-V)}{\epsilon\log\epsilon}, \tag{2.28}$$

respectively. The time-averaged power is then

$$\overline{\mathscr{P}} \sim 4\pi \int_0^1 \left[\epsilon^2\overline{U^2} + \frac{\overline{W^2}}{2\log(1/\epsilon)}\right] \mathrm{d}z. \tag{2.29}$$

Hence, the efficiency is

$$\eta = \frac{D}{\overline{\mathscr{P}}} \sim \frac{1}{2}\overline{V}^2 \left[\int_0^1 \left(\overline{W^2} + 2\epsilon^2\overline{U^2}\log\frac{1}{\epsilon}\right)\mathrm{d}z\right]^{-1}. \tag{2.30}$$

3. Non-deforming prolate spheroids

We now apply the slender-body results to situations in which the swimmer has fixed shape, but the fluid at its surface has a prescribed velocity or stress. We focus on prolate spheroids, with $R \equiv \sqrt{\Delta} = \sqrt{4z(1-z)}$, and establish a connection with some existing models from the literature. The integral equation (2.14) now becomes

$$\mathscr{S}[\Lambda] \equiv -(2\log\epsilon + 1)\Lambda + \int_0^1 [\Lambda(z') - \Lambda(z)]\frac{\mathrm{d}z'}{|z'-z|} = W - V + \frac{\partial\delta}{\partial z}. \tag{3.1}$$

https://doi.org/10.1017/jfm.2014.120 Published online by Cambridge University Press

3.1. *Keller and Wu's 'porous swimmer'*

Instead of solving (3.1) for Λ, we first assume that this density is constant and then determine the corresponding surface velocity field. We find

$$\Lambda = -2\epsilon^2 V_n, \quad U = -V_n R_z, \quad W = V_s \quad \text{and} \quad V = V_s - 4\epsilon^2 V_n \log\epsilon, \tag{3.2}$$

in terms of two parameters, V_n and V_s, which is the slender-body limit of Keller & Wu's (1977) model. Note that the radial velocity in (3.2) is singular at the ends of the swimmer, calling into question the validity of the solution. To resolve this issue properly, one must proceed deeper into the slender-body asymptotics, which requires revision at the ends (Tillett 1970; Johnson 1980).

3.2. *'Tank-treading' and 'jetting'*

If U is finite at the ends of the prolate spheroid then $\delta(0) = \delta(1) = 0$, and (2.16) reduces to

$$V = \int_0^1 W(z)\,\mathrm{d}z. \tag{3.3}$$

Thus, the locomotion speed is determined independently of the integral equation (3.1). The 'tank-treading' model of Leshansky *et al.* (2007) poses a tangential surface velocity, $V_t(z)$, without any normal flow. In the slender geometry, this amounts to prescribing $V_t(z) \approx W(z)$; the locomotion speed then follows immediately from (3.3), which is the limiting form of the result provided by Leshansky *et al.*, expressed in the current notation.

If we impose a given normal surface velocity, $V_n(z)$, without any tangential flow, we recover the 'jetting' model of Spagnolie & Lauga (2010). To order ϵ^2, we have

$$U = V_n(z) \quad \text{and} \quad W = -\epsilon^2 R_z V_n(z) \tag{3.4}$$

(given the definition $u(\epsilon R, z) = \epsilon U(z)$). Thus,

$$V = -\epsilon^2 \int_0^1 R_z V_n\,\mathrm{d}z, \tag{3.5}$$

which corresponds to Spagnolie & Lauga's result for a slender prolate spheroid.

Leshansky *et al.* (2007) and Spagnolie & Lauga (2010) determined the efficiencies of these locomotive strategies. We do not follow suit here, as the results can be extracted from these earlier works by taking the slender limit. However, the results ignore dissipation inside the swimmer, which may be critical, especially for the jetting problem, in which viscous fluid must flow through a porous matrix within the organism. Even in the simpler situation in which the body is a fluid-filled shell and pumps at the surface generate normal flow, the internal dissipation still dominates, as illustrated in the model outlined in the Appendix.

3.3. *Fixed traction models*

A number of models treat the organism as having a fixed shape with no normal flow and a prescribed surface traction (Saintillan & Shelley 2007; Kanevsky *et al.* 2010). In our slender geometry, the surface shear stress is dominated by $w_r \sim -2\Lambda/(\epsilon R)$

https://doi.org/10.1017/jfm.2014.120 Published online by Cambridge University Press

(using (2.15)). Thus, as a parallel, we take $U=\delta=0$ and prescribe $\Lambda(z)$. For specific examples, one can make use of the identity (Tuck 1964; Blake *et al.* 2010)

$$\mathscr{S}[P_n(s)] = -(2\log\epsilon + 1 + \lambda_n)P_n(s), \quad \lambda_n = 2\sum_{j=1}^{n} j^{-1}, \quad s = 2z-1, \tag{3.6}$$

where $P_n(s)$ is a Legendre polynomial of degree $n>0$. If

$$\Lambda = \sum_{n=1}^{\infty} \Lambda_n P_n(s) \quad \text{and} \quad \sum_{n=1}^{\infty} \Lambda_{2n} = \sum_{n=1}^{\infty} \Lambda_{2n-1} = 0, \tag{3.7}$$

there is no net force on the swimmer ($\int_0^1 \alpha\,\mathrm{d}z = \frac{1}{2}\int_0^1 \Lambda\,\mathrm{d}z = 0$), and the shear stress is finite at the ends ($\Lambda \to 0$ for $z=0$ and 1). Furthermore, on demanding that $W(z)$ also vanish at the ends,

$$W = V - (2\log\epsilon + 1)\Lambda - \sum_{n=1}^{\infty} \lambda_n \Lambda_n P_n \quad \text{and} \quad V = \sum_{n=1}^{\infty} \lambda_{2n}\Lambda_{2n}, \tag{3.8}$$

provided $\sum_{n=1}^{\infty} \lambda_{2n-1}\Lambda_{2n-1} = 0$.

The model used by Saintillan & Shelley (2007) and Kanevsky *et al.* (2010) corresponds to a shear-stress distribution of $\Delta = \sqrt{4z(1-z)} = \sqrt{1-s^2}$, or $\Lambda = 1-s^2$, which cannot satisfy the no-net-force condition. Indeed, the axial velocity solutions displayed by Kanevsky *et al.* (2010) suggest the development of boundary-layer structure at the swimmer's ends in the slender limit, which is not captured by our model. An alternative simple illustration is provided by

$$\Lambda = P_2(s) - P_4(s) = \tfrac{7}{8}(1-s^2)(1-5s^2), \tag{3.9}$$

for which

$$W = \tfrac{7}{48}(125s^2 - 13)(s^2-1) - (2\log\epsilon + 1)\Lambda \quad \text{and} \quad V = -\tfrac{7}{6}. \tag{3.10}$$

4. Models with prescribed surface deformation

We next consider surface waves as the activators of locomotion, assuming that the surface is impermeable, without slip, and has prescribed time-dependent deformations. By way of a simple model, we consider surface motions for which an element originally located at the position $(f(\varsigma), \varsigma)$ is shifted to $(R(z,t), z)$, where

$$R(z,t) = f(\varsigma) + \theta a(\varsigma)\sin\phi, \quad z = \varsigma + \chi a(\varsigma)\sin(\phi - \Phi), \tag{4.1}$$

and $f(\varsigma)$ denotes the undeformed radius of the swimmer (Blake 1971*b*). Here, θ and χ are the amplitudes of the transverse and longitudinal wave components (respectively), both of which are characterised by the wavenumber k, phase ϕ and envelope $a(\varsigma)$, with

$$\phi = k(\varsigma - t) \quad \text{and} \quad \int_0^1 a^2\,\mathrm{d}z = 1. \tag{4.2}$$

The components are phase-shifted from one another by Φ. The surface velocity is

$$U = -k\theta a\cos\phi \quad \text{and} \quad W = -k\chi a\cos(\phi - \Phi) \tag{4.3}$$

(see Blake 1971*b*). Note that the radial displacement implied by (4.1) is $O(\epsilon)$; to avoid the axial displacement (which is $O(\chi)$) from being unrealistically much larger, and to simplify the analysis, we therefore take $\chi \ll 1$, and specifically of order ϵ or smaller.

https://doi.org/10.1017/jfm.2014.120 Published online by Cambridge University Press

We compute the integrals in the time average of (2.19) to leading order (after changing the integration variable from z to ς, and including $\partial z/\partial\varsigma$ within the time average):

$$\int_0^1 \overline{W\frac{\partial z}{\partial\varsigma}}\,\mathrm{d}\varsigma = -k\chi\int_0^1 \overline{(1+\chi a_\varsigma\sin\hat{\phi}+k\chi a\cos\hat{\phi})a\cos\hat{\phi}}\,\mathrm{d}\varsigma = -\frac{1}{2}k^2\chi^2, \tag{4.4}$$

where $\hat{\phi}=\phi-\Phi$,

$$\begin{aligned}
&-\frac{1}{2\log\epsilon}\int_0^1 \overline{W\frac{\partial z}{\partial\varsigma}\log\frac{R^2}{\Delta}}\,\mathrm{d}\varsigma\\
&\quad\sim\frac{k\chi}{\log\epsilon}\int_0^1 \overline{\cos(\phi-\Phi)\log(f+\theta a\sin\phi)}a\,\mathrm{d}\varsigma\\
&\quad=\frac{k\chi\theta\sin\Phi}{\log\epsilon}\int_0^1\frac{\overline{\cos^2\phi}}{f+\theta a\sin\phi}a^2\,\mathrm{d}\varsigma=\frac{k\chi\sin\Phi}{\theta\log\epsilon}\int_0^1\left[f-\sqrt{f^2-\theta^2a^2}\right]\mathrm{d}\varsigma
\end{aligned} \tag{4.5}$$

and

$$\frac{\epsilon^2}{4\log\epsilon}\int_0^1\overline{(RU)_z\frac{\partial z}{\partial\varsigma}\log\frac{R^2}{\Delta}}\,\mathrm{d}\varsigma\sim\frac{\epsilon^2k^2\theta^2}{4\log\epsilon}. \tag{4.6}$$

Thus, we obtain

$$\overline{V}\sim-\frac{\epsilon^2k^2\theta^2}{4\log\epsilon}-\frac{1}{2}k^2\chi^2+\frac{k\chi\sin\Phi}{\theta\log\epsilon}\int_0^1\left[f-\sqrt{f^2-\theta^2a^2}\right]\mathrm{d}\varsigma. \tag{4.7}$$

Similar calculations with (2.30) establish that the leading-order efficiency is

$$\eta\sim\frac{2\overline{V}^2}{k^2(\chi^2-2\epsilon^2\theta^2\log\epsilon)}. \tag{4.8}$$

When the surface motion is purely transverse ($\chi\to0$), we have

$$\overline{V}=\frac{\epsilon^2k^2\theta^2}{4\log(1/\epsilon)}\quad\text{and}\quad\eta=\frac{k^2\epsilon^2\theta^2}{16[\log(1/\epsilon)]^3}\quad\text{(transverse waves)}. \tag{4.9}$$

Conversely, when the longitudinal wave component dominates ($\theta\to0$), we find that

$$\overline{V}\sim-\tfrac{1}{2}k^2\chi^2\quad\text{and}\quad\eta\sim\tfrac{1}{2}k^2\chi^2\quad\text{(longitudinal waves)}. \tag{4.10}$$

In other words, longitudinal waves drive the swimmer in the opposite direction to transverse waves (cf. Tuck 1968; Blake 1971*a*), and are more efficient for comparable amplitudes of surface deformation (i.e. $\chi=O(\epsilon)$). The mechanism by which purely longitudinal wave motion activates locomotion is elucidated by the term in (4.4), which can be written in terms of the average, $\overline{\zeta_\varsigma\zeta_t}$, where ζ is the fluid displacement, $\zeta=z-\varsigma$. This represents a steady streaming flow due to the propagating longitudinal waves that generates a mean translation speed even for a planar boundary (see Tuck 1968; Blake 1971*b*).

For low-amplitude uniform waves on a cylinder, $\theta\ll1$, $f=a=1$, and (4.7) becomes

$$\overline{V}\sim\frac{\epsilon^2k^2\theta^2}{4\log(1/\epsilon)}-\frac{1}{2}k^2\chi^2+\frac{k\chi\theta\sin\Phi}{2\log\epsilon}, \tag{4.11}$$

https://doi.org/10.1017/jfm.2014.120 Published online by Cambridge University Press

which is equivalent to Blake's (1971*b*) result for a cylinder with small radius. Blake's leading-order speed is, in the current notation,

$$V_{Blake} = \frac{1}{2}k^2\theta^2\left[\frac{\epsilon k(\mathrm{K}_1^2 - \mathrm{K}_0^2) - 2\chi\epsilon\mathrm{K}_1^2\sin\Phi}{2\mathrm{K}_1\mathrm{K}_0 - \epsilon k(\mathrm{K}_1^2 - \mathrm{K}_0^2)} - \chi^2\right], \tag{4.12}$$

where $\mathrm{K}_0 = \mathrm{K}_0(\epsilon k)$ and $\mathrm{K}_1 = \mathrm{K}_1(\epsilon k)$ are modified Bessel functions of the second kind. With $\chi = 0$, this also corresponds to Setter *et al.*'s (2012) result for transverse waves. Taking the limit $\epsilon k \to 0$, we recover (4.11). Note that there is an inconsistency in applying our slender-body theory to a cylinder, as we assumed that $R \to 0$ at the ends. However, the slender-body result still holds when the swimmer is not quite cylindrical, but has narrow edge layers over which the radius decreases from unity to zero; the corrections from the edge layers are smaller than the leading-order result in (4.11).

It is clear from (4.7) that the speed of a slender axisymmetrical swimmer driven by surface waves is insensitive to both the shape of the swimmer, $f(z)$, and the wave profile, $a(z)$: only through the final 'cross'-term in (4.7) does either attribute enter the final result. Thus, with either pure transverse or longitudinal waves, cylinders swim as fast as prolate spheroids or other shapes given the same wave forcing and maximum radius. Moreover, swimmers receive the same thrust whether the surface waves are spatially localised or evenly spread (given the normalisation (4.2)). Our result for the swimming speed in (4.7) is also equally valid for linear or nonlinear changes in shape; that is, for wave motions that are stronger than Taylor's classical limit. These observations justify the use of previous results for low-amplitude waves on spheres or other shapes to estimate swimming speeds for a wide variety of model swimmers, provided one includes the correct dependence on aspect ratio, which is $\epsilon^2/\log\epsilon$ for transverse waves (cf. Ehlers *et al.* 1996; Ehlers & Oster 2012; Setter & Bucher 2014).

Despite this, models that prescribe the surface deformation are unphysical at higher amplitudes: for $\theta \to \mathrm{Max}(a/f)$, the swimmer becomes constricted at certain axial positions where internal stresses would undoubtedly limit the surface deformation. The model in (4.1) also does not conserve volume; if the interior of the swimmer was filled with an incompressible fluid, the internal pressure would prevent such surface deformations unless the surface was permeable (cf. Arroyo *et al.* 2012). Rather than fabricate an alternative to (4.1) that limits constrictions and conserves volume, in § 5 we consider the internal fluid mechanics in detail, assuming the swimmer to be a fluid-filled elastic shell.

5. Internal peristaltic dynamics

Adopting a prescribed form for the surface velocity ignores the mechanics underlying how the corresponding deformations are generated. Moreover, the efficiencies of the swimming strokes determined above are potentially incorrect because the dissipation inside the swimmer is ignored. To avoid both limitations, in this section we formulate a model that incorporates internal flow and surface mechanics, assuming that the swimmer consists of an elastic shell filled with viscous fluid. The model is closely connected to models of peristalsis (Takagi & Balmforth 2011), and is also relevant to studies of internal transport and mixing (Iima & Nakagaki 2012; Alim *et al.* 2013) and other pressure-driven internal flows within organisms (Charras *et al.* 2005; Charras & Palluch 2008).

5.1. *Lubrication analysis*

Given the small aspect ratio and slow motions, we use lubrication theory to describe the internal flow dynamics. To pave the way, we introduce some new variables suited

https://doi.org/10.1017/jfm.2014.120 Published online by Cambridge University Press

to the fluid interior: first, inside the swimmer $r = O(\epsilon)$; second, the aspect ratio and surface motion indicate that $u = O(\epsilon)$, whereas mass conservation demands that w is $O(1)$; last, we rescale pressure in accordance with the main force balance. Hence, we set

$$r = \epsilon\rho, \quad u = \epsilon v(\rho, z, t), \quad w = w(\rho, z, t), \quad P = \epsilon^{-2}\frac{\mu_I}{\mu}p(\rho, z, t), \tag{5.1}$$

where μ_I is the viscosity of the internal fluid. The leading-order lubrication equations that stem from the internal versions of (2.1) are then

$$\frac{1}{\rho}\frac{\partial(\rho v)}{\partial\rho} + \frac{\partial w}{\partial z} = 0, \tag{5.2}$$

$$\frac{\partial p}{\partial\rho} = 0 \quad \text{and} \quad \frac{\partial p}{\partial z} = \frac{1}{\rho}\frac{\partial}{\partial\rho}\left(\rho\frac{\partial w}{\partial\rho}\right). \tag{5.3}$$

Thus $p = p(z, t)$ and the second relation in (5.3) can be integrated to give

$$w(\rho, z, t) = W(z, t) + \frac{1}{4}\frac{\partial p}{\partial z}(\rho^2 - R^2). \tag{5.4}$$

In conjunction with the surface boundary condition, $u(R, z, t) = R_t + WR_z$, the radial integral of the continuity (5.2) then furnishes

$$\frac{\partial}{\partial t}(R^2) + \frac{\partial}{\partial z}(R^2 W) = \frac{1}{8}\frac{\partial}{\partial z}\left(R^4\frac{\partial p}{\partial z}\right). \tag{5.5}$$

The dissipation rate inside the swimmer is given, to leading order, by

$$\mathscr{P}_I = 2\pi\int_0^1\int_0^R \rho\left(\frac{\partial w}{\partial\rho}\right)^2 \mathrm{d}\rho\,\mathrm{d}z \equiv \frac{\pi}{8}\int_0^1\left(\frac{\partial p}{\partial z}\right)^2 R^4\,\mathrm{d}z. \tag{5.6}$$

This is of order one if the pressure gradient is also of that order, and is larger than the external dissipation rate in (2.25) by a factor of either ϵ^{-2} or $1/\log\epsilon$ depending on the form of the surface motion. Hence, the efficiency is better redefined as $\eta = D/\overline{\mathscr{P}_I}$, and is rather smaller than the estimates provided earlier.

5.2. *Dynamics of an elastic shell*

Our model for the surface of the swimmer is a thin elastic shell acted upon by the forces from the fluid interior and exterior, and by a set of 'muscle fibres' that actuate motion. We use classical membrane theory to represent the resistance of the shell (Timoshenko & Woinowsky-Kreiger 1959): an element that is initially at position $(f(\varsigma), \varsigma)$ is deformed to $(R(z, t), z)$, where $z = \varsigma + \zeta$ and ζ is the axial displacement. Ignoring the shell's inertia and in terms of the Lagrangian coordinate ς, the force balance on the surface is

$$\mathscr{F}_r = \frac{\lambda}{f}\left(\frac{R - f}{f} - \nu\frac{\partial\zeta}{\partial\varsigma}\right), \tag{5.7}$$

$$\mathscr{F}_z = \frac{\epsilon}{f}\frac{\partial}{\partial\varsigma}\left[\lambda f\left(\nu\frac{R - f}{f} - \frac{\partial\zeta}{\partial\varsigma}\right)\right], \tag{5.8}$$

https://doi.org/10.1017/jfm.2014.120 Published online by Cambridge University Press

where $(\mathscr{F}_r, \mathscr{F}_z)$ is the combination of fluid and fibre forces, per unit area, λ is an elastic modulus and ν is Poisson's ratio. Here, to make the equations dimensionless, we have scaled both with $\mu_I c/\epsilon^2 L$ (the internal pressure scale), in which case $\lambda \equiv \epsilon Eh/(1-\nu^2)\mu_I c$, where h is the shell's thickness and E is Young's modulus.

In view of the rescaling in (5.1), the pressure inside the swimmer is $O(\epsilon^{-2})$ higher than outside, assuming that the viscosity ratio is $O(1)$. Moreover, in our slender geometry, the normal fluid force is dominated by that pressure. Thus, the radial force balance trades off the lubrication pressure and fibre force against the solid mechanical tension that maintains the surface structure. Denoting the *inward* fibre force by $\mathscr{T}$, we find

$$\check{p} = \mathscr{T} + \frac{\lambda}{f}\left(\frac{R-f}{f} - \nu\frac{\partial \zeta}{\partial \varsigma}\right), \tag{5.9}$$

where $\check{p}(\varsigma, t)$ denotes the fluid pressure force in the Lagrangian frame. The forcing $\mathscr{T}$ could be provided by a network of muscle fibres that are stretched diametrically across each cross-section of the swimmer, with a density that is sufficient to exert an axisymmetrical force on the surface, but thin enough so that the viscous internal fluid flow is not impeded. However, the detailed origin of $\mathscr{T}$ is not critical to the model; all that matters is that a radial force is exerted on the elastic shell to activate motion.

To leading order, and in the Eulerian frame described by z, the axial force exerted on the surface by the internal fluid is $-\epsilon(\tau + pR_z)$, where

$$\tau = \left[\frac{\partial w}{\partial \rho}\right]_{\rho=R} \equiv \frac{1}{2}R\frac{\partial p}{\partial z} \tag{5.10}$$

is the surface shear stress. To estimate the corresponding stress exerted by the external fluid, we note that the near-surface external velocity field in (2.15) implies that the local shear stress is dominated by $w_\rho \sim O(\Lambda)$, with $\Lambda \sim -W/(2\log\epsilon)$ following from the integral equation. Thus, the external shear stress is $O(1/\log\epsilon)$ smaller than τ and can again be neglected. This leaves the axial traction of the internal fluid, $-\epsilon(\tau + pR_z)$, which we denote by $-\epsilon\check{\tau}(\varsigma, t)$, when converted to the Lagrangian frame.

The axial fibre forcing could be provided by a network of muscles or molecular motors embedded within the shell. These fibres pull surface elements together or apart in such a way as to create the longitudinal wave. However, the fibres cannot exert any net axial force on the swimmer, a condition equivalent to demanding that the corresponding contribution to $\int_0^1 f\mathscr{F}_z\,\mathrm{d}\varsigma$ must vanish. We therefore introduce the forcing via the density, $\mathscr{V}(\varsigma, t)$, in

$$\mathscr{F}_z \sim -\check{\tau} + \frac{\epsilon}{f}\frac{\partial \mathscr{V}}{\partial \varsigma}, \tag{5.11}$$

with $\mathscr{V}(0,t) = \mathscr{V}(1,t) = 0$. Thus,

$$\check{\tau} = \frac{1}{f}\frac{\partial}{\partial \varsigma}\left[\mathscr{V} + \lambda f\left(\frac{\partial \zeta}{\partial \varsigma} + \nu\frac{f-R}{f}\right)\right]. \tag{5.12}$$

Note that one can actuate surface deformation in the model in different ways than through the explicit fibre forces represented by $\mathscr{T}$ and $\mathscr{V}$. For example, one could also produce surface motions by modulating the elastic modulus λ in situations where the internal pressure is elevated and the surface is under tension. Locomotion is then actuated without using surface spring forces, but by changing the surface structure, which might be more suitable for certain organisms. Local weakenings of the surface layer might also be useful for modelling the pressure-driven flows occurring during the blebbing of cells (Charras *et al.* 2005; Charras & Palluch 2008).

https://doi.org/10.1017/jfm.2014.120 Published online by Cambridge University Press

5.3. *Simple transverse waves*

For simple transverse waves, we assume that the muscle network within the elastic shell is sufficient to suppress any tangential motion, $\zeta = W = 0$ (so there is no difference between the Eulerian and Lagrangian coordinates, z and ς). The axial force balance in (5.12) is then irrelevant and the radial force balance becomes

$$p = D(R - f) + \Theta A(z)\sin\phi, \quad \phi = k(z - t), \tag{5.13}$$

where $D = \lambda/f^2$ is an effective radial stiffness, and we have taken a specific form for the muscular forcing $\mathscr{T}$, involving a sinusoidal pattern with amplitude Θ, axial envelope $A(z)$ and wavenumber k. Equations (5.5) and (5.13) now furnish an evolution equation for the profile of the travelling surface waves driven by the actuating fibre force. This problem is similar to the peristaltic flow problem considered by Takagi & Balmforth (2011). Moreover, it is decoupled from the external locomotion problem owing to the mismatch in the internal and external pressures; given the solution of (5.5) and (5.13), we compute the mean locomotion speed from (2.22).

In (5.13), two limits of the stiffness parameter have particular significance: when $D \to 0$, the forcing immediately determines the fluid pressure, $p \sim \Theta A \sin z$, which then reorganises the fluid and determines the surface shape according to (5.5). For $D \gg 1$ and $\Theta = O(D)$, the forcing directly dictates the radius, as in § 4, unless lubrication pressures become so large as to upset the balance between the terms on the right-hand side of (5.13). Such an outcome is likely when the leading-order radius, $R \sim f - (\Theta A/D)\sin z$, does not conserve volume or becomes too constricted.

5.3.1. *Initial-value problems*

The lubrication theory suggests the initial-value problem,

$$\frac{\partial}{\partial t}(R^2) = \frac{1}{8}\frac{\partial}{\partial z}\left(R^4\frac{\partial p}{\partial z}\right), \quad p = D(R - f) + \Theta A(z)\sin\phi, \quad R(z, 0) = f(z), \tag{5.14}$$

modelling how the swimmer profile evolves once the forcing is switched on at $t = 0$. We solve this problem numerically by discretising z on a uniform grid and approximating spatial derivatives using centred differences. The evolution equation is then turned into a set of coupled ordinary differential equations (ODEs) for the radius at each grid point, which are solved using a standard stiff time integrator. To ensure that pressure gradients do not build up at the front and back of the swimmer (which may cause the ends to shift axially), we stiffen the swimmer there by locally increasing $D(z)$ and decreasing the forcing envelope $A(z)$; elsewhere, D is taken constant. For practical purposes, we mostly use $D = \cosh[4^5(z - \frac{1}{2})^8]$ and $A \propto D^{-1}$. This procedure enforces $R \to f$ and removes any fluid flux near the ends.

A sample solution to the initial-value problem is shown in figure 1, for a prolate spheroid ($f = \sqrt{4z(1 - z)}$) with a proportionate forcing envelope ($A = f/D$), amplitude $\Theta = 1/8$ and wavenumber $k = 20$ (generating about three wave crests over the swimmer's length). The forcing generates rightward-travelling waves over the swimmer's surface that drive the object towards the left (i.e. $V > 0$, given our choice of reference frame). After a transient, the solution converges to a periodic state. Notably, the waves induce a mean rearrangement of the swimmer's interior, pushing a fraction of the fluid to the back end.

Periodic swimming states for different forcing amplitudes and wavenumbers are shown in figure 2, illustrating the effect on both the wave profiles and the mean

https://doi.org/10.1017/jfm.2014.120 Published online by Cambridge University Press

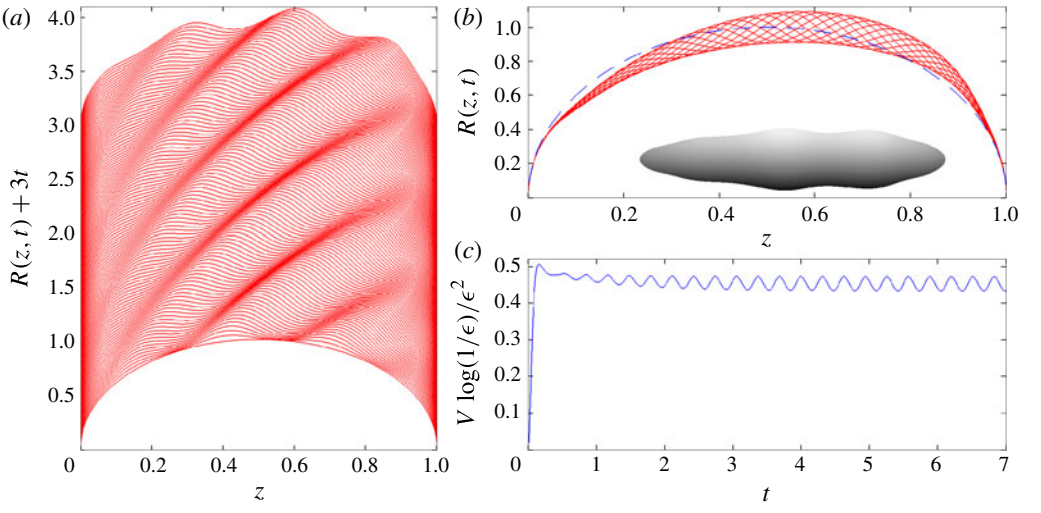


FIGURE 1. (Colour online) A solution of the initial-value problem (5.14) for a prolate spheroid ($f = \sqrt{4z(1-z)}$) with a stiffness $D = \cosh[4^5(z - \frac{1}{2})^8]$, forced by waves with envelope $A = f/D$, wavenumber $k = 20$ and amplitude $\Theta = 1/8$: (*a*) snapshots of $R(z, t)$ every 0.01 time units, offset vertically by $3t$; (*b*) ten snapshots of the limiting periodic motion; and (*c*) a time series of the instantaneous scaled locomotion speed, $V\log(1/\epsilon)/\epsilon^2$, from (2.19). The inset greyscale image in panel (*b*) illustrates the appearance of the swimmer's surface.

deformation. The mean swimming speeds, $\overline{V}$ in (2.22), and efficiencies, $\eta \equiv 2\pi\overline{V}^2/\overline{\mathscr{P}_I}\log(1/\epsilon)$, extracted from suites of such solutions are plotted against forcing amplitude in figure 3. The dependence on ϵ is removed in the plots by scaling $\overline{V}$ by $\epsilon^2/\log(1/\epsilon)$ and η by $\epsilon^4/\log(1/\epsilon)$. Except for higher forcing amplitudes, these data highlight how the dominant dependence of the locomotion speed is on the combination $k^2\Theta^2$; the efficiency depends chiefly on $k^4\Theta^2$. At the higher forcings, the permanent deformation induced by the locomotive waves complicates the situation in a manner that depends on how we stiffen the ends of the swimmer (which controls the degree of thinning of the forward sections; see figure 2).

A lower-wavenumber higher-amplitude solution is shown in figure 4. Interestingly, despite the relatively simple fashion in which the system is forced, the swimming stroke takes the form of a fairly complex spatio-temporal pattern. During the periods of maximum forcing, a distinct localised bulge develops that propagates from the head to the tail of the swimmer. The bulge then subsides as the forcing wanes, with the pressure build-up at the tail rapidly driving the internal fluid back to the head. Finally, the forcing builds back up to re-establish the bulge and repeat the pattern. The instantaneous swimming speed varies significantly throughout the cycle, with the rapid pressure-driven backflow actually propelling the swimmer backwards even though the mean progress is forwards (see figure 4*b*). The swimming stroke and gait resemble the locomotion strategy of the *Eutreptiella* cell (Fletcher & Theriot 2004; Aroyo *et al.* 2012), illustrating how a seemingly complicated biological stroke might have a relatively simple underlying mechanism (cf. Allard & Mogilner 2013). Nevertheless, although the virtues of our model include its simplicity, there are clear limitations in the comparison to real biological organisms like *Eutreptiella* cells. In particular, the length of the swimmer is fixed in the model, but the relative motion

https://doi.org/10.1017/jfm.2014.120 Published online by Cambridge University Press

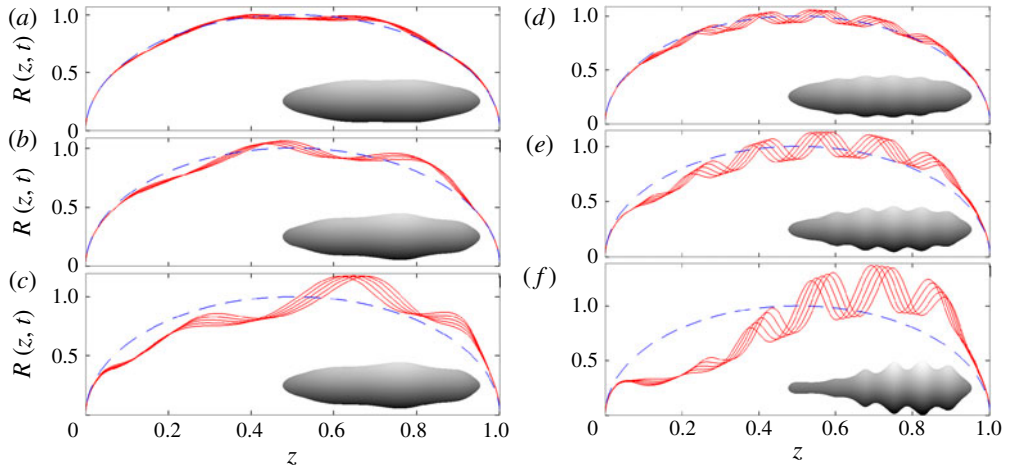


FIGURE 2. (Colour online) Surface profiles for a prolate spheroid ($f = \sqrt{4z(1-z)}$) with a stiffness $D = \cosh[4^5(z-\frac{1}{2})^8]$, forced by waves with envelope $A = f/D$: (*a*)–(*c*) with $k = 15$ and forcing amplitudes of $\Theta = 1/16$, $1/8$ and $1/4$, respectively; (*d*)–(*f*) with $k = 40$ and the same forcing strengths. For each case, four equally spaced snapshots are shown; the dashed line shows the undeformed swimmer. Again, the inset greyscale images illustrate the appearance of the swimmer's surface.

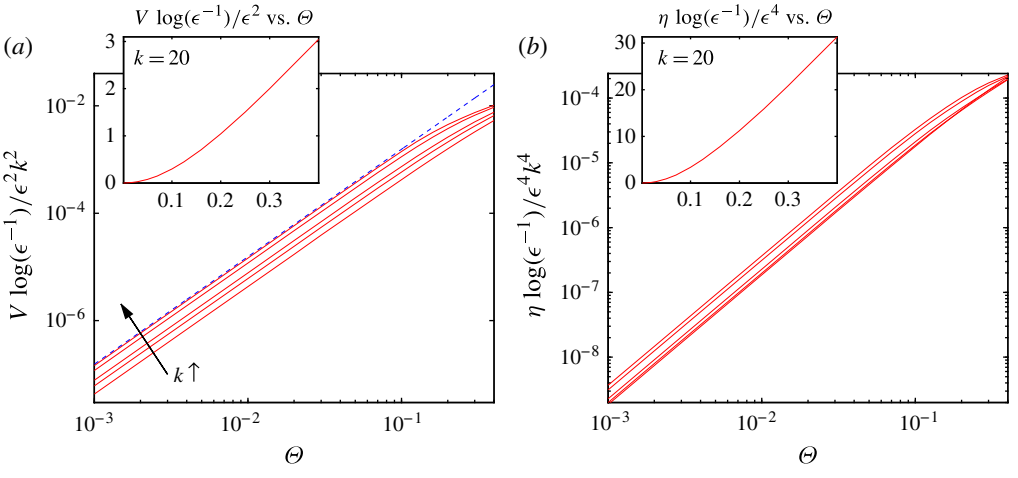


FIGURE 3. (Colour online) (*a*) Scaled mean locomotion speeds and (*b*) efficiencies. (*a*) Plot of $\overline{V}\log(1/\epsilon)/\epsilon^2 k^2$ against Θ for $k = 10$, 15, 20, 40 and 100. The dashed line shows the prediction in (5.24). The inset shows $\overline{V}\log(1/\epsilon)/\epsilon^2$ against Θ for $k = 20$. (*b*) Plot of $\eta\log(1/\epsilon)/\epsilon^4 k^4$, for the same values of k as in panel (*a*), where $\eta = 2\pi\overline{V}^2/\mathscr{P}_I \log(1/\epsilon)$. The inset shows $\eta\log(1/\epsilon)/\epsilon^4$ against Θ for $k = 20$.

of the ends of the actual organism may be significant, and the surface structure and motion are more convoluted than in our model (Arroyo *et al.* 2012).

5.3.2. *Short-wavelength solutions*

Analytical approximations of the periodic locomoting states are available for small wavelengths, $k \gg 1$ (but not so small that $k \sim \epsilon^{-1}$, which would violate our

https://doi.org/10.1017/jfm.2014.120 Published online by Cambridge University Press

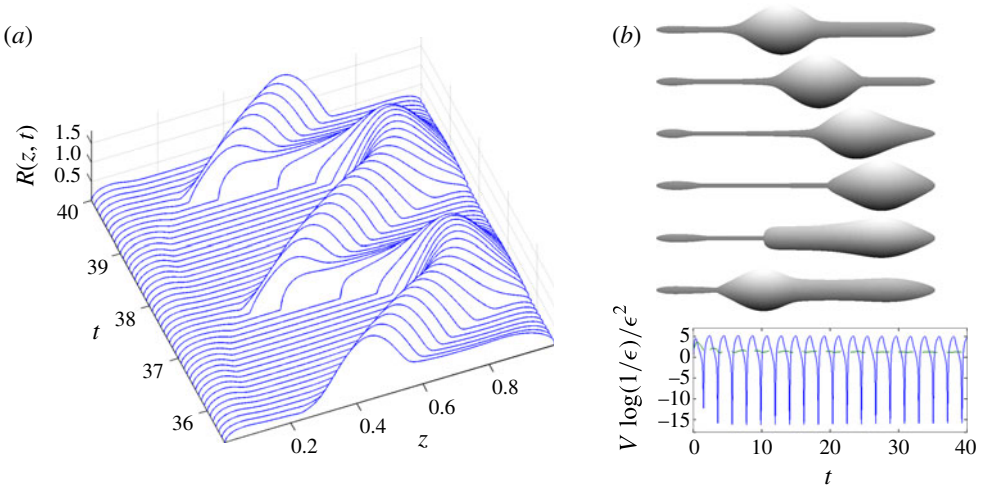


FIGURE 4. (Colour online) Solution to the initial-value problem (5.14) for a prolate spheroid, $f = \Delta$, with $k = 3$ and $\theta = 10$. In this example, the stiffness is $D = 1 + 200[\mathrm{e}^{-\sqrt{x}/0.1} + \mathrm{e}^{-\sqrt{1-x}/0.1}]$. (*a*) A space–time plot of the radius $R(z, t)$ once the solution has converged to its final periodic state. (*b*) Sample images of the surface profile, along with the instantaneous scaled locomotion speed (solid) and its running average (dashed).

slender-body asymptotics). The analysis amounts to an application of multiple scale theory, searching for a solution depending on the fast scales, kt and kz, and the slow scale, z. In particular, the long-time periodic solution of (5.14) depends on the fast scales through the combination ϕ. Hence, to extract analytical solutions in this limit, we first introduce the change of variable, $(z, t) \to (z, \phi)$, which furnishes

$$2kRR_\phi = \tfrac{1}{8}(k\partial_\phi + \partial_z)[R^4(k\partial_\phi + \partial_z)p]. \tag{5.15}$$

We next pose the asymptotic sequences,

$$R = R_0 + k^{-1}R_1 + \cdots \quad \text{and} \quad p = p_0 + k^{-1}p_1 + \cdots . \tag{5.16}$$

We find, at $O(k^2)$,

$$(R_0^4 p_{0\phi})_\phi = 0 \quad \text{or} \quad p_{0\phi} = \frac{C_0(z)}{R_0^4}. \tag{5.17}$$

But, $\overline{p_{0\phi}} = 0$ and $\overline{R_0^{-4}} \neq 0$, where $\overline{(\cdots)} \equiv [1/(2\pi)] \int_0^{2\pi} (\cdots)\, \mathrm{d}\phi$. Hence, $C_0 = 0$, and so

$$R_0 = F + \frac{\Theta A}{D} \sin\phi \quad \text{and} \quad p_0 = D(F - f), \tag{5.18}$$

where $F(z) \equiv \overline{R_0}$ and must be found by proceeding to higher order.

At $O(k)$, we find

$$-8(R_0^2)_\phi = (R_0^4 p_{1\phi})_\phi + (R_0^4 p_{0z})_\phi \quad \text{or} \quad C_1(z) - 8R_0^2 = R_0^4 p_{1\phi} + R_0^4 p_{0z}. \tag{5.19}$$

At $O(1)$, the phase average of the PDE indicates that

$$\frac{\mathrm{d}J}{\mathrm{d}z} = -\frac{1}{8}\frac{\mathrm{d}}{\mathrm{d}z}\left(\overline{R_0^4 p_{1\phi}} + \overline{R_0^4 p_{0z}}\right) = 0. \tag{5.20}$$

https://doi.org/10.1017/jfm.2014.120 Published online by Cambridge University Press

Here, J is the leading-order phase-averaged axial flux, which must vanish given the impermeable ends of the swimmer. Thus, we have

$$C_1 \equiv 8\overline{R_0^2} \equiv 8(1+\tfrac{1}{2}\alpha^2)F^2, \quad \alpha = \frac{\Theta A}{DF}. \tag{5.21}$$

The phase average of $p_{1\phi}$ from (5.19), in combination with (5.18), now provides an equation for the mean radius:

$$\frac{\mathrm{d}}{\mathrm{d}z}[D(F-f)] = 8\overline{R_0^2}\,\overline{R_0^{-4}} - 8\overline{R_0^{-2}} = \frac{2\alpha^2(16-\alpha^2)}{F^2(1-\alpha^2)^{7/2}}. \tag{5.22}$$

Equation (5.22) can be solved subject to the constraint $\int_0^1 (F^2 - f^2)\,\mathrm{d}z = 0$, stemming from mass conservation. If the ends of the swimmer are stiffened, and the edge layers are not too thin in comparison to the wavelength $2\pi/k$, then the equation can be solved over the interval $0 < z < 1$ with $D = D(z)$. Numerical solutions of (5.22) derived in this way are compared with periodic states of the initial-value problem in figure 5. For the stiffening chosen, the edge layers are fairly narrow, leading to some discrepancies between the short-wavelength and initial-value solutions near the front of the swimmer. Alternatively, if the stiffening increases sharply at positions, $z = z_e$ and $1 - z_e$, displaced a finite distance from the ends, one can solve (5.22) over $z_e < z < 1 - z_e$ with constant D, imposing $\int_{z_e}^{1-z_e} (F^2 - f^2)\,\mathrm{d}z = 0$. This alternative solution is also plotted in figure 5.

The leading-order solution for $k \gg 1$ is therefore

$$R \sim F(1 + \alpha \sin\phi) = F + \frac{\Theta A}{D}\sin\phi. \tag{5.23}$$

The waves therefore drive a mean locomotion speed of

$$\overline{V} = \frac{\epsilon^2}{2\log\epsilon}\int_0^1 \overline{R_t R_z}\,\mathrm{d}z \sim \frac{\epsilon^2 k^2}{2\log(1/\epsilon)}\int_0^1 \overline{R_\phi^2}\,\mathrm{d}z \sim \frac{\epsilon^2 k^2 \Theta^2}{4\log(1/\epsilon)}\int_0^1 \frac{A^2}{D^2}\,\mathrm{d}z, \tag{5.24}$$

which is compared with numerical data in figure 3(*a*). If the swimmer ends were not stiffened, D a constant and $A = f = \sqrt{4z(1-z)}$, then (5.24) furnishes the simpler result, $\overline{V} \sim -\epsilon^2 k^2 \Theta^2/(6D^2\log\epsilon)$. Also, the pressure solution indicates that the power input $\mathscr{P}_I$ in (5.6) remains $O(1)$ for $k \gg 1$, whereas $\overline{V} \propto k^2$, leading to the expectation that $\eta \propto k^4$, as observed numerically in figure 3(*b*).

Note that the zero-flux condition, $J \equiv -\frac{1}{8}\overline{R_0^4(p_{0z} + p_{1\phi})} = 0$, helps to elucidate the mean deformation of the swimmer evident in the numerical computations. This deformation reflects the leading-order pressure, $p \sim p_0 = D(F-f)$, which drives a net flux $\frac{1}{8}\overline{R_0^4 p_{0z}}$ from the tail to the head of the swimmer (see figure 5*c*). That reverse flux is set up to balance the net forward transport induced by the peristaltic waves (as given by $-\frac{1}{8}\overline{R_0^4 p_{1\phi}}$), because fluid cannot flow through the ends of the swimmer. Such pressure-driven flows have been observed in *Physarum plasmodium*, which propels itself using surface contractions (Matsumoto, Takagi & Nakagaki 2008). Much as in our model, the surface motions of this organism have also been claimed to be actuated by molecular 'springs'.

5.3.3. *Opening the ends*

In the preceding model, the internal fluid is peristaltically pumped within a closed chamber (as in the rectangular ducts of, for example, Selverov & Stone (2001) and Yi *et al.* (2002)). The transverse surface waves are thereby the means to drive external

https://doi.org/10.1017/jfm.2014.120 Published online by Cambridge University Press

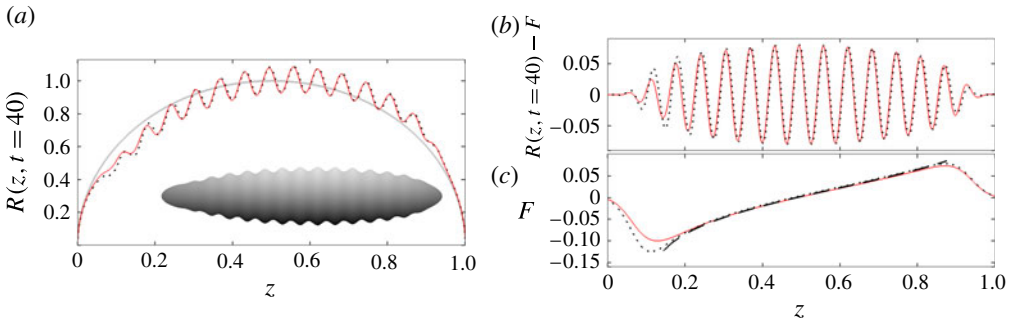


FIGURE 5. (Colour online) Comparison of short-wavelength theory and numerical solution of the initial-value problem for $k = 100$ and $\Theta = 0.08$, and remaining parameters as in figure 1. (*a*) The solution at $t = 40$; the light grey line shows the unperturbed profile of the swimmer. (*b*) The mean radius of the swimmer from the initial-value problem (the time-averaged radius over $10 < t < 40$) is subtracted from $R(z, t = 40)$ and compared to $(\Theta A/D)\sin\phi$. (*c*) Comparison of that mean radius with F. In all the panels, the solid lines represent the solution of the initial-value problem and the dotted line shows the short-wavelength predictions, incorporating the variation of D over the stiffened ends (see main text). In panel (*c*), the dashed line shows the short-wavelength result assuming that the stiffening of the ends abruptly switches on at $z = 1/8$ and $7/8$.

fluid flow and actuate locomotion. The situation is quite different, however, when the ends of the swimmer are open and fluid can be peristaltically pumped through the swimmer's body, as we illustrate next. For the task, we again solve (5.14), but now applying the boundary conditions, $p(0, t) = p(1, t) = 0$, given that lubrication pressures within the swimmer remain much larger than external fluid pressures (cf. (5.1)). We use an unperturbed surface profile $f(z)$ that is finite at the ends, and use a uniform stiffness (constant D). A sample solution for a cylinder ($f = 1$) is shown in figure 6. The configuration is now more like a standard peristaltic pumping problem (e.g. Shapiro *et al.* 1969; Jaffrin & Shapiro 1971), although the specific forcing and dynamics of the elastic surface are distinct from traditional models of peristalsis (see Takagi & Balmforth 2011). The model is also now more like that proposed by Ajdari & Stone (1999), or a hybrid that combines surface waves and jetting (Spagnolie & Lauga (2010); see also the Appendix).

Analytical predictions can again be provided in the short-wavelength limit: the analysis proceeds much as before, except that $J \neq 0$ in view of the finite flux. Hence the constant in (5.19) is $C_1 \equiv 8[(1 + \frac{1}{2}\alpha^2)F^2 - J]$, and the mean amplitude satisfies

$$\frac{\mathrm{d}p_0}{\mathrm{d}z} = D\frac{\mathrm{d}}{\mathrm{d}z}(F - f) = 8\left[\left(\overline{R_0^2} - J\right)\overline{R_0^{-4}} - \overline{R_0^{-2}}\right] = \frac{2\alpha^2(16 - \alpha^2)}{F^2(1 - \alpha^2)^{7/2}} - \frac{4J(2 + 3\alpha^2)}{F^4(1 - \alpha^2)^{7/2}}, \quad (5.25)$$

with $p_0 \to 0$ (or $F \to f$) to either end of the swimmer. Hence,

$$J = \frac{\langle \alpha^2(16 - \alpha^2)F^{-2}(1 - \alpha^2)^{-7/2}\rangle}{2\langle (2 + 3\alpha^2)F^{-4}(1 - \alpha^2)^{-7/2}\rangle}, \quad \text{where } \langle\cdots\rangle \equiv \int_0^1 (\cdots)\,\mathrm{d}z. \quad (5.26)$$

For small amplitudes $\Theta \ll 1$, $F \sim 1 + O(\Theta)$, $\alpha^2 = O(\Theta^2)$ and $J \sim 4\langle\alpha^2\rangle \sim 4\Theta^2\langle A^2\rangle/D^2$. The short-wavelength predictions obtained from solving (5.25) are included for

https://doi.org/10.1017/jfm.2014.120 Published online by Cambridge University Press

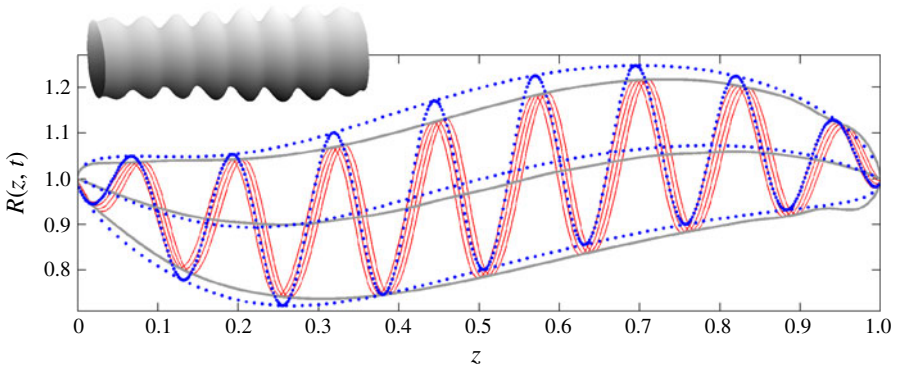


FIGURE 6. (Colour online) Numerical solution of the initial-value problem for an open-ended cylinder, forced with an amplitude of $\Theta = 0.2$, wavenumber $k = 50$ and envelope $A = \Delta$, $D = 1$. Three snapshots of the numerical solution are shown (thin red full lines, including that at $t = 40$) after the system has converged to its periodic state; the light grey lines show the envelope and mean of the surface waves. The dots show corresponding results for the short-wavelength theory (F, $F \pm \Theta\Delta$ and the reconstruction of $R(z, t = 40)$). The phase-averaged flux of the numerical solution, $-\overline{R^4 p_z}/8$, is 0.09 (or 0.100 and 0.103 for $k = 100$ and 200, respectively), the short-wavelength prediction being $J = 0.104 \approx 8\Theta^2/3$.

comparison with the solution of the initial-value problem in figure 6; in this example, the flux $J \approx 4\Theta^2\langle A^2\rangle = \frac{8}{3}\Theta^2$.

To determine the swimming speed, we observe from (2.19) that any mean axial flow along the swimmer's surface dominates transverse motions in driving locomotion (by $O(\epsilon^2/\log\epsilon)$). The peristaltic flux, J, pumped through the swimmer constitutes exactly such a mean axial flow, and so we conclude that $\overline{V} \sim J = O(\Theta^2)$. This speed is substantially larger than that predicted by (5.24) for transverse waves, illustrating how the permeability of the swimmer's ends is critical. (It should be noted that the slender-body theory assumes that the radius of the body vanishes at the ends of the swimmer, and is not strictly valid for an open-ended arrangement. Instead, one could modify the model so that the swimmer's radius vanishes at the ends, and allow local flow into the interior through a permeable surface, or refine the slender-body analysis to accommodate the open ends.)

5.4. *Simple longitudinal waves*

To model simple longitudinal waves, we assume that the radial forcing $\mathscr{T}$ is sufficient to suppress any radial motion of the surface, so $R(z, t) = f(\varsigma)$ and $U = \partial R/\partial t = 0$. The radial force balance in (5.13) then becomes redundant and the evolution equation (5.5) integrated to furnish

$$\frac{\partial p}{\partial z} = \frac{8W}{f^2}. \tag{5.27}$$

The axial displacement ζ is now the key dynamical variable of the model. To determine an evolution equation for this variable, we use the Eulerian frame (z, t), and write the axial kinematic condition,

$$W = \frac{\partial \zeta}{\partial t} + W\frac{\partial \zeta}{\partial z}. \tag{5.28}$$

https://doi.org/10.1017/jfm.2014.120 Published online by Cambridge University Press

Further progress is hampered by the need to transform between the Eulerian and Lagrangian frames of reference, indexed by z and ς, respectively, to determine the surface strains and impose the axial force balance in (5.12). To simplify the situation, we therefore make the additional approximation that the forcing amplitude is sufficiently small that $|\zeta| \ll 1$. To leading order, we therefore take $\varsigma \approx z$ and ignore the distinction between the two frames. Thence, (5.12) reduces to

$$\frac{1}{2}\frac{\partial}{\partial z}(f^2 p) = \frac{\partial}{\partial z}\left(\mathscr{V} + \lambda f \frac{\partial \zeta}{\partial z}\right), \tag{5.29}$$

Integrating (5.29), substituting the result into (5.27) and then using $W \approx \partial\zeta/\partial t$, implies

$$\frac{\partial \zeta}{\partial t} = \frac{1}{4} f^2 \frac{\partial}{\partial z}\left(\chi A \sin\phi + D_T \frac{\partial \zeta}{\partial z}\right), \tag{5.30}$$

where $D_T = \lambda/f$ is an effective axial stiffness, and we have adopted the model forcing,

$$\mathscr{V} = k\chi f^2 A(z) \sin k(z - t). \tag{5.31}$$

The amplitude here contains an additional factor of k to ensure that the solution for ζ presented below scales with k and χ as in Blake's model of § 4.

To solve for the long-time periodic solutions to (5.30), we may set $\zeta = \gamma(z)\cos\phi + \varpi(z)\sin\phi$, which turns that equation into a pair of coupled ODEs for the amplitudes, $\gamma(z)$ and $\varpi(z)$. Rather than proceed down that route, we consider short wavelengths, $k \gg 1$. In this limit, the spatial derivatives of ϕ dominate in (5.30), and we find

$$\zeta \sim \frac{\chi A}{D_T}\cos\phi. \tag{5.32}$$

For the locomotion speed, we observe that the kinematic condition implies, to leading order in ζ, that

$$\overline{V} = \int_0^1 \overline{W}\,\mathrm{d}z \sim \int_0^1 \overline{\zeta_z \zeta_t}\,\mathrm{d}z \tag{5.33}$$

(cf. (4.4) and the discussion in § 4). For $k \gg 1$, using (5.32), this reduces to

$$\overline{V} \sim -\frac{1}{2}k^2\chi^2 \int_0^1 \frac{A^2}{D_T^2}\,\mathrm{d}z, \tag{5.34}$$

which is analogous to (4.11) with $\theta = 0$. A short calculation indicates that

$$\overline{\mathscr{P}_I} = 8\pi \int_0^1 \overline{W^2}\,\mathrm{d}z \sim 4\pi k^2\chi^2 \int_0^1 \frac{A^2}{D_T^2}\,\mathrm{d}z \tag{5.35}$$

in the same limit. Hence the efficiency is

$$\eta = \frac{k^2\chi^2}{8\log(1/\epsilon)} \int_0^1 \frac{A^2}{D_T^2}\,\mathrm{d}z. \tag{5.36}$$

A comparison of (5.34) with the corresponding result for transverse waves in (5.24), for comparable amplitudes of surface deformation (i.e. $\chi = O(\epsilon)$) indicates that the

https://doi.org/10.1017/jfm.2014.120 Published online by Cambridge University Press

locomotion speed $\overline{V}$ is $O(\log\epsilon)$ faster for longitudinal waves. Moreover, the efficiency in (5.36) is $O(\epsilon^{-1}\log\epsilon)^2$ larger than that for transverse waves. Two effects conspire for these differences: first, transverse waves drive external fluid flow differently to longitudinal waves with slender geometry, leading to the differing factor of $\log\epsilon$ in the locomotion speed; second, the internal dissipation rate is $O(\epsilon^2)$ smaller for longitudinal waves when $\chi = O(\epsilon)$ because the internal shear rates are then $O(\epsilon)$ smaller.

6. Discussion

In this study we have modelled the locomotion of an axisymmetric slender body propelled by motions of its surface. For such geometry, slender-body theory provides a compact integral formula for the locomotion speed in terms of the surface velocity. We focused specifically on the case of travelling surface waves, and calculated locomotion speeds when the profiles of these waves were prescribed. Our results indicate how the aspect ratio of the swimmer factors into the locomotion speed, and justifies the use of previous results for low-amplitude waves on spheres to estimate swimming speeds, as has been done previously for *Synechococcus* (Ehlers *et al.* 1996; Ehlers & Oster 2012).

Models with prescribed surface motion suffer from the drawback that they ignore the internal mechanics of the swimmer. This is especially problematic for the definition of an efficiency characterising the swimming stroke because, in slender geometries, the dissipation occurring inside the swimmer may well be much larger than that arising from the external flow. To circumvent these issues, we formulated a model for the internal fluid mechanics, treating the swimmer as a solid, but deformable, shell filled with viscous fluid. In this model, the locomotive waves are generated by exerting forces on the surface, and lubrication theory determines the resulting internal fluid flow and surface deformation. A key feature of the analysis is that, provided the contrast between the internal and external viscosities is not severe, the internal lubrication forces dominate the stresses exerted on the swimmer by the external flow. As a result, the locomotion problem decouples from the internal flow dynamics and it is straightforward to determine the efficiency of the swimming stroke.

Our results suggest that transverse waves are not an efficient strategy for locomotion when compared to longitudinal waves, especially when internal fluid dissipation is taken into account. The efficiency of transverse waves is improved if fluid can be pumped through the swimmer's body (swimming by swallowing), which is feasible if the interior can be hollowed out or if the innards can be mixed with the external fluid. Though intriguing for the design of robotic swimmers, these results raise the question of why any micro-organism would adopt transverse surface waves as a means of propulsion. On the other hand, an elastic shell filled with viscous fluid may not be an ideal biological model. Similarly, energetic efficiency may not be the main control on the style of swimming, adhesive locomotion over a substrate being a preferred mode (e.g. Barry & Bretscher 2010; Van Haastert 2011) or the need to transport nutrients, catch prey or detect chemical and thermal gradients being more demanding (e.g. Magar, Goto & Pedley 2003; Short *et al.* 2006; Guasto, Rusconi & Stocker 2012; Michelin & Lauga 2013).

Slender organisms that do, in fact, appear to use a type of transverse surface wave for propulsion are amoeboid cells (Barry & Bretscher 2010; Van Haastert 2011; Driscoll *et al.* 2012; Farutin *et al.* 2013; Howe, Barry & Bretscher 2013). These cells more typically move by adhesive locomotion. However, when freely suspended

https://doi.org/10.1017/jfm.2014.120 Published online by Cambridge University Press

in fluid, they have been observed to swim using propagating surface protrusions ('pseudopods'). As a simple application of the results of § 4, we make a brief comparison with observations of *Dictyostelium* cells (Van Haastert 2011): the aspect ratio of these cells is of the order of 1/5, and their length is of the order of 0.02 mm; at any particular moment, Van Haastert observes that approximately three pseudopods, of amplitude 10^{-3} mm and speed 2×10^{-4} mm s^{-1}, drive the cell forwards. Hence, we estimate $k \approx 20$ and $\theta \approx 1/4$, and so the predicted locomotion speed from (4.7) is 3×10^{-5} mm s^{-1}, which is close to the observed speed of 5×10^{-5} mm s^{-1}. Of course, the pseudopods are not axisymmetrical surface distortions but localised bulbous protrusions, suggesting that the prediction might be too large. On the other hand, the protrusions are also not sinusoidal in shape, and their effective wavelength is rather smaller than one-third of the swimmer's length (implying a higher value for k). Closer to the geometry of our model is the swimming stroke of *Eutreptiella* cells, which use nearly axisymmetrical surface waves to propel themselves (Fletcher & Theriot 2004); in fact, the wave patterns and gait of this organism are surprisingly similar to some of our model solutions.

Unless the innards of the swimmer deform far more easily than the external fluid, the severe penalty associated with internal dissipation is likely to be critical to a number of other locomotion strategies. For example, the 'push-me-pull-you' model of Avron, Kenneth & Oaknin (2005) considers an organism with two bulbous sections connected by a narrow conduit. The swimming stroke requires that the internal material is redistributed between the two sections at different instants during the swimming stroke by forcing flow through the conduit. As already noted by Avron *et al.*, this action unavoidably generates a much higher internal dissipation than that occurring in the external fluid.

Such considerations lead one to wonder what locomotive strategies might minimise the internal dissipation. A key point is that the peristaltic model of § 5 assumes that surface forces drive significant radial shear in the internal axial velocity (i.e. $\partial w/\partial r = O(c/\epsilon L)$). If, instead, the forcing drives a purely extensional internal flow with relatively little radial shear, the internal dissipation is lower by $O(\epsilon^2)$ (the dissipation rate is now given by the volume average of terms such as $|\partial w/\partial z|^2 = O(c^2/L^2)$), and therefore no longer dominates the external dissipation. In other words, if one can avoid peristalsis (defined as pressure-driven internal shear flow) whilst suitably rearranging the swimmer's body, excessive internal dissipation may be avoided. It is not difficult to envision how one might achieve such a protocol in the multi-sphere models of Najafi & Golestanian (2004), Felderhof (2006) and others (see Lauga & Powers 2009), given that the interior is mostly confined to rigid spheres and swimming is activated by extending or contracting the narrow conduits that connect them. To verify this, one could conduct a detailed analysis of the efficiency of such models following along the guidelines set out in our current study.

Other possible extensions of our model include adding a more complicated internal constitution for the swimmer. Biological organisms can be composed of complex fluids, viscoelastic solids or poroelastic media, and one could try to replace the viscous interior of our model accordingly. For the cyanobacteria *Synechococcus* (Ehlers & Oster 2012) and *Myxococcus xanthus* (Nan & Zusman 2011), it would also be worth while to consider more complicated surface motions, such as helical waves of both normal and tangential displacement (see also Palagi *et al.* 2013).

To avoid one major limitation of our analysis, one might seek generalisations that allow the ends of the swimmer to move relative to one another. Without that extension, the model cannot be used to explore the dynamics of locomotion strategies

https://doi.org/10.1017/jfm.2014.120 Published online by Cambridge University Press

in which length variations may play an important role, such as the blebbing of cells. The formation of a bleb is itself a result of pressure-driven flow within a cell, arising from the local weakening of the material in the cell wall (Charras *et al.* 2005; Charras & Palluch 2008). To study this process in more detail, one could employ an interesting variant of our model in which local reductions in surface stiffness in conjunction with an elevated internal pressure drive surface deformation without the need for any embedded spring forces (one could also devise locomotion strategies based on propagating waves using this device).

Lastly, one might consider related optimisation problems, such as how to select the shape of the undeformed swimmer or the envelope of the forcing in order to maximise the locomotion speed (e.g. Wilkening & Hosoi 2008, Walker & Shelley 2010). In fact, it is perhaps a little disappointing that our results actually suggest that the swimming speed is relatively insensitive to these characteristics.

Acknowledgements

This work started at the 2012 Geophysical Fluid Dynamics Summer Program, Woods Hole Oceanographic Institution, which is supported by the National Science Foundation and the Office of Naval Research. We thank the participants for discussions, particularly J. B. Keller and W. R. Young. We also thank J. S. Wettlaufer. S.T. thanks Yale University and the University of Oxford for financial support during the course of this work. We thank the referees for their constructive criticisms, which helped us to improve the manuscript.

Appendix A. Internal jetting dynamics

Consider a shell filled with viscous fluid. The shell contains openings fitted with 'pumps' that drive normal fluid flow. By suitably forcing the pumps, we can engineer a jetting flow through the swimmer. The surface boundary conditions are, to leading order,

$$U = V_n \quad \text{and} \quad W = -\epsilon^2 V_n R_z, \tag{A 1}$$

where $V_n(z)$ is the normal fluid speed. Hence, the internal fluid flow is

$$w = -\frac{1}{4}\frac{\partial p}{\partial z}(R^2 - \rho^2). \tag{A 2}$$

The radial integral of the continuity equation demands that

$$\frac{\partial q}{\partial z} \equiv RV_n = -\frac{\partial}{\partial z}\int_0^R w\rho \,\mathrm{d}\rho = \frac{1}{16}\frac{\partial}{\partial z}\left(R^4\frac{\partial p}{\partial z}\right), \tag{A 3}$$

where q is the internal fluid flux. Thus,

$$\frac{\partial p}{\partial z} = \frac{16q}{R^4} \quad \text{or} \quad p = 16\int_0^z \frac{q\,\mathrm{d}\hat{z}}{R^4}. \tag{A 4}$$

For a specific illustration, we consider the prolate spheroid, $R = \Delta$, and assume that the forcing establishes a flux, $q = R^\alpha$, for some parameter α. Then,

$$\frac{\partial p}{\partial z} = 16R^{\alpha-4}, \quad V_n = \alpha R^{\alpha-2}\frac{\mathrm{d}R}{\mathrm{d}z} = 2\alpha[4z(1-z)]^{(\alpha-3)/2}(1-2z) \tag{A 5}$$

https://doi.org/10.1017/jfm.2014.120 Published online by Cambridge University Press

and

$$V = \int_0^1 W \,\mathrm{d}z = -\frac{4\alpha\epsilon^2}{\alpha - 2} I_{\alpha-2}, \quad I_j = \int_0^1 R^j \,\mathrm{d}z = \frac{2^j \Gamma(1 + \frac{1}{2}j)^2}{\Gamma(2 + j)}. \tag{A 6}$$

If we ignore the internal dissipation, as in (2.30), the efficiency is

$$\eta \sim -\frac{4\epsilon^2 I_{\alpha-2}^2}{(\alpha - 2) I_{2\alpha-4} \log \epsilon}. \tag{A 7}$$

However, the internal dissipation is rather larger than that occurring outside the swimmer, and a better measure of efficiency is

$$\eta_I \sim -\frac{\alpha^2 \epsilon^4 I_{\alpha-2}^2}{(\alpha - 2)^2 I_{2\alpha-4} \log \epsilon}, \tag{A 8}$$

which is $O(\epsilon^2)$ smaller than that in (A 7).

REFERENCES

AJDARI, A. & STONE, H. A. 1999 A note on swimming using internally generated travelling waves. *Phys. Fluids* **11**, 1275–1277.

ALIM, K., AMSELEM, G., PEAUDECERF, F., BRENNER, M. P. & PRINGLE, A. 2013 Random network peristalsis in *Physarum polycephalum* organises fluid flows across an individual. *Proc. Natl Acad. Sci. USA* **110** (33), 13 306–13 311.

ALLARD, J. & MOGILNER, A. 2013 Traveling waves in actin dynamics and cell motility. *Curr. Opin. Cell Biol.* **25**, 107–115.

ARROYO, M., HELTAI, L., MILLÁN, D. & DESIMONE, A. 2012 Reverse engineering the euglenoid movement. *Proc. Natl Acad. Sci. USA* **109** (44), 17874–17879.

AVRON, J. E., KENNETH, O. & OAKNIN, D. H. 2005 Pushmepullyou: An efficient micro-swimmer. *New J. Phys.* **7** (1), 234.

BARRY, N. P. & BRETSCHER, M. S. 2010 *Dictyostelium* amoebae and neutrophils can swim. *Proc. Natl Acad. Sci. USA* **107** (25), 11 376–11 380.

BLAKE, J. R. 1971*a* A spherical envelope approach to ciliary propulsion. *J. Fluid Mech.* **46** (2), 199–208.

BLAKE, J. R. 1971*b* Infinite models for ciliary propulsion. *J. Fluid Mech.* **49** (2), 209–222.

BLAKE, J. R. 1971*c* Self-propulsion due to oscillations on the surface of a cylinder at low Reynolds numbers. *Bull. Austral. Math. Soc.* **5**, 255–264.

BLAKE, J. R., TUCK, E. O. & WAKELEY, P. W. 2010 A note on the *S*-transform and slender-body theory in Stokes flow. *IMA J. Appl. Maths* **75**, 343–355.

BRAHAMSHA, B. 1999 Non-flagellar swimming in marine *Synechococcus*. *J. Mol. Microbiol. Biotechnol.* **1** (1), 59–62.

CHARRAS, G. & PALLUCH, E. 2008 Blebs lead the way: how to migrate without lamellipodia. *Nat. Rev. Mol. Cell Biol.* **9**, 730–736.

CHARRAS, G. T., YARROW, J. C., HORTON, M. A., MAHADEVAN, L. & MITCHISON, T. J. 2005 Non-equilibration of hydrostatic pressure in blebbing cells. *Nat. Lett.* **435**, 365–369.

CHILDRESS, S. 1981 *Mechanics of Swimming and Flying*. Cambridge University Press.

COX, R. G. 1970 The motion of long slender bodies in a viscous fluid. Part 1. General theory. *J. Fluid Mech.* **44** (4), 791–810.

DRISCOLL, M. K., MCCANN, C., KOPACE, R., HOMAN, T., FOURKAS, J. T., PARENT, C. & LOSERT, W. 2012 Cell shape dynamics: from waves to migration. *PLoS Comput. Biol.* **8** (3), e1002392.

EHLERS, K. & OSTER, G. 2012 On the mysterious propulsion of *Synechococcus*. *PLoS One* **7** (5), e36081.

EHLERS, K. M., SAMUEL, A. D. T., BERG, H. C. & MONTOGOMERY, R. 1996 Do cyanobacteria swim using traveling surface waves? *Proc. Natl Acad. Sci. USA* **93**, 8340–8343.

https://doi.org/10.1017/jfm.2014.120 Published online by Cambridge University Press

FARUTIN, A., RAFAI, S., DYSTHE, D. K., DUPERRAY, A., PEYLA, P. & MISBAH, C. 2013 Amoeboid swimming: a generic self-propulsion of cells in fluids by means of membrane deformations. *Phys. Rev. Lett.* **111**, 228102.

FELDERHOF, B. U. 2006 The swimming of animalcules. *Phys. Fluids* **18**, 063101.

FLETCHER, D. A. & THERIOT, J. A. 2004 An introduction to cell motility for the physical scientist. *Phys. Biol.* **1** (1), T1.

GUASTO, J. S., RUSCONI, R. & STOCKER, R. 2012 Fluid mechanics of planktonic microorganisms. *Annu. Rev. Fluid Mech.* **44**, 373–400.

HOWE, J. D., BARRY, N. P. & BRETSCHER, M. S. 2013 How do amoebae swim and crawl? *PLoS One* **8** (9), e74382.

IIMA, M. & NAKAGAKI, T. 2012 Peristaltic transport and mixing of cytosol through the whole body of *Physarum plasmodium*. *Math. Med. Biol.* **29** (3), 263–281.

JAFFRIN, M. Y. & SHAPIRO, A. H. 1971 Peristaltic pumping. *Annu. Rev. Fluid Mech.* **3**, 13–37.

JARRELL, K. F. & MCBRIDE, M. J. 2008 The surprisingly diverse ways that prokaryotes move. *Nat. Rev. Microbiol.* **6**, 466–476.

JOHNSON, R. E. 1980 An improved slender-body theory for Stokes flow. *J. Fluid Mech.* **99** (2), 411–431.

KANEVSKY, A., SHELLEY, M. J. & TORNBERG, A.-K. 2010 Modelling simple locomotors in Stokes flow. *J. Comput. Phys.* **229**, 958–977.

KELLER, J. B. & RUBINOW, S. I. 1976 Slender-body theory for slow viscous flow. *J. Fluid Mech.* **75**, 705–714.

KELLER, S. R. & WU, T. Y. 1977 A porous prolate-spheroidal model for ciliated micro-organisms. *J. Fluid Mech.* **80** (2), 259–278.

LAUGA, E. & POWERS, T. 2009 The hydrodynamics of swimming microorganisms. *Rep. Prog. Phys.* **72**, 1–36.

LESHANSKY, A. M., KENNETH, O., GAT, O. & AVRON, J. E. 2007 A frictionless microswimmer. *New J. Phys.* **9**, 145–162.

LIGHTHILL, M. J. 1952 On the squirming motion of nearly spherical deformable bodies through liquids at very small Reynolds numbers. *Commun. Pure Appl. Maths* **109**, 109–118.

MAGAR, V., GOTO, T. & PEDLEY, T. J. 2003 Nutrient uptake by a self-propelled steady squirmer. *Q. J. Mech. Appl. Maths* **56**, 65–91.

MATSUMOTO, K., TAKAGI, S. & NAKAGAKI, T. 2008 Locomotive mechanism of *Physarum plasmodia* based on spatiotemporal analysis of protoplasmic streaming. *Biophys. J.* **94**, 2492–2504.

MICHELIN, S. & LAUGA, E. 2013 Unsteady feeding and optimal strokes of model ciliates. *J. Fluid Mech.* **715**, 1–31.

NAJAFI, A. & GOLESTANIAN, R. 2004 Simple swimmer at low Reynolds number: three linked spheres. *Phys. Rev.* E **69** (6), 062901.

NAKAHARA, K., YAMAMOTO, M., OKAYAMA, Y., YOSHIMURA, K., FUKAGATA, K. & MIKI, N. 2013 A peristaltic micropump using travelling waves on a polymer membrane. *J. Micromech. Microengng* **23** (8), 085024.

NAN, B. & ZUSMAN, D. R. 2011 Uncovering the mystery of gliding motility in the Myxobacteria. *Annu. Rev. Genet.* **45**, 21–39.

PALAGI, S., JAGER, E. W., MAZZOLAI, B. & BECCAI, L. 2013 Propulsion of swimming microrobots inspired by metachronal waves in ciliates: from biology to material specifications. *Bioinspir. Biomim.* **8** (4), 046004.

SAINTILLAN, D. & SHELLEY, M. J. 2007 Orientational order and instabilities in suspensions of self-locomoting rods. *Phys. Rev. Lett.* **99**, 058102.

SELVEROV, K. P. & STONE, H. A. 2001 Peristaltically driven channel flows with applications toward micromixing. *Phys. Fluids* **13**, 1837–1859.

SETTER, E. & BUCHER, I. 2013 Robotic swimmer/pump based on an optimal wave generating mechanism. *Mech. Mach. Theory* **70**, 266–277.

SETTER, E. & BUCHER, I. 2014 Elastic travelling waves in multi-dimensional structures with application to self-propulsion. In *Proc. ISMA2010, September 2010, Leuven, Belgium* (ed. P. Sas & B. Bergen), KU Leuven.

https://doi.org/10.1017/jfm.2014.120 Published online by Cambridge University Press

SETTER, E., BUCHER, I. & HABER, S. 2012 Low-Reynolds-number swimmer utilising surface travelling waves: analytical and experimental study. *Phys. Rev.* E **85**, 066304.

SHAPIRO, A. H., JAFFRIN, M. Y. & WEINBERG, S. L. 1969 Peristaltic pumping with long wavelengths at low Reynolds number. *J. Fluid Mech.* **37**, 799–825.

SHORT, M. B., SOLARI, C. A., GANGULY, S., POWERS, T. R., KESSLER, J. O. & GOLDSTEIN, R. E. 2006 Flows driven by flagella of multicellular organisms enhance long-range molecular transport. *Proc. Natl Acad. Sci. USA* **103** (22), 8315–8319.

SPAGNOLIE, S. E. & LAUGA, E. 2010 Jet propulsion without inertia. *Phys. Fluids* **22**, 081902.

STONE, H. A. & SAMUEL, A. D. T. 1996 Propulsion of microorganisms by surface distortions. *Phys. Rev. Lett.* **77** (19), 4102–4104.

STONE, H. A., STROOCK, A. D. & AJDARI, A. 2004 Engineering flows in small devices: microfluidics toward a lab-on-a-chip. *Annu. Rev. Fluid Mech.* **36**, 381–411.

TAKAGI, D. & BALMFORTH, N. J. 2011 Peristaltic pumping of viscous fluid in an elastic tube. *J. Fluid Mech.* **672**, 196–218.

TAYLOR, G. I. 1951 Analysis of the swimming of microorganisms. *Proc. R. Soc. Lond.* A **209**, 447–461.

TILLETT, J. P. K. 1970 Axial and transverse Stokes flow past slender axisymmetric bodies. *J. Fluid Mech.* **44** (3), 401–417.

TIMOSHENKO, S. & WOINOWSKY-KREIGER, S. 1959 *Theory of Plates and Shells*. McGraw-Hill.

TUCK, O. E. 1964 Some methods for flow past blunt slender bodies. *J. Fluid Mech.* **18**, 619–635.

TUCK, O. E. 1968 A note on a swimming problem. *J. Fluid Mech.* **31**, 305–308.

VAN HAASTERT, P. J. M. 2011 Amoeboid cells use protrusions for walking, gliding and swimming. *PLoS One* **6**, e27532.

WALKER, S. W. & SHELLEY, M. J. 2010 Shape optimization of peristaltic pumping. *J. Comput. Phys.* **229**, 1260–1291.

WILKENING, J. & HOSOI, A. E. 2008 Shape optimization of swimming sheets. *J. Fluid Mech.* **601**, 25–61.

YI, M., BAU, H. H. & HU, H. 2002 Peristaltically induced motion in a closed cavity with two vibrating walls. *Phys. Fluids* **14**, 184–197.

https://doi.org/10.1017/jfm.2014.120 Published online by Cambridge University Press